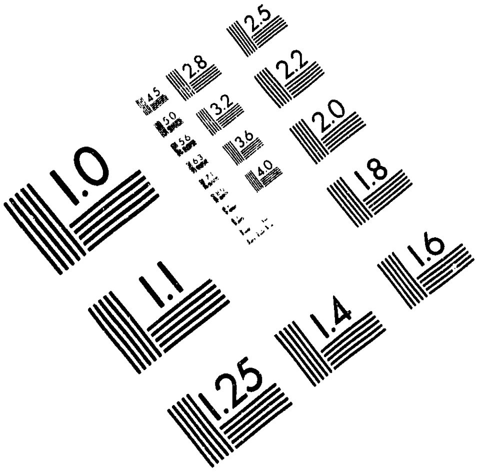

AIIM

Association for Information and Image Management

1100 Wayne Avenue, Suite 1100
Silver Spring, Maryland 20910
301/587-8202

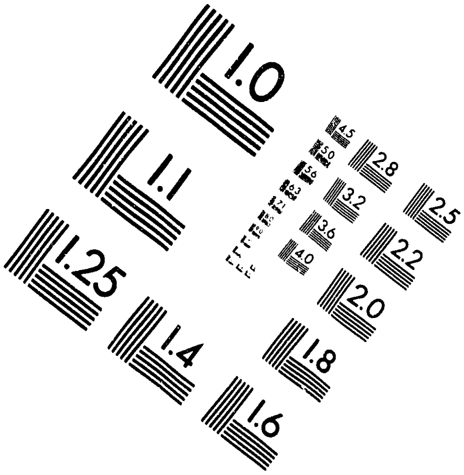

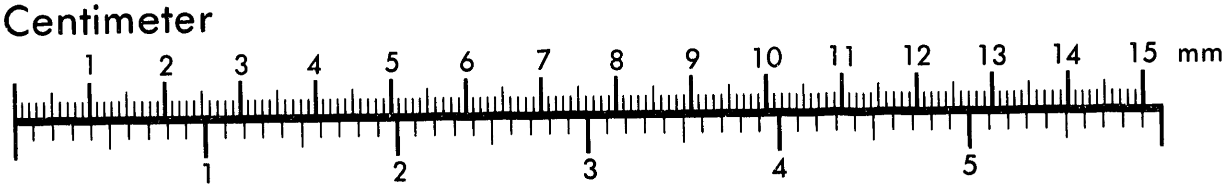

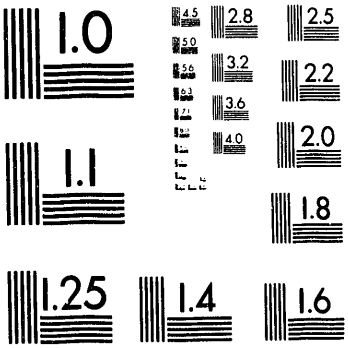

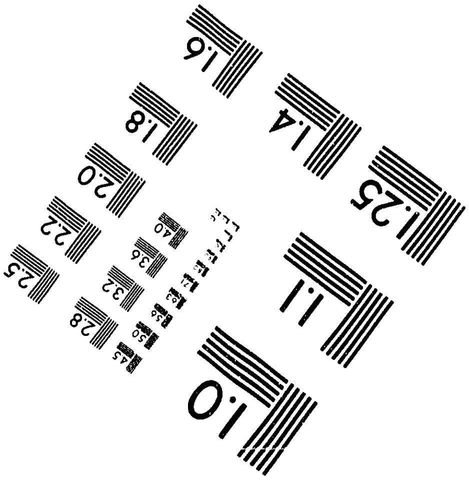

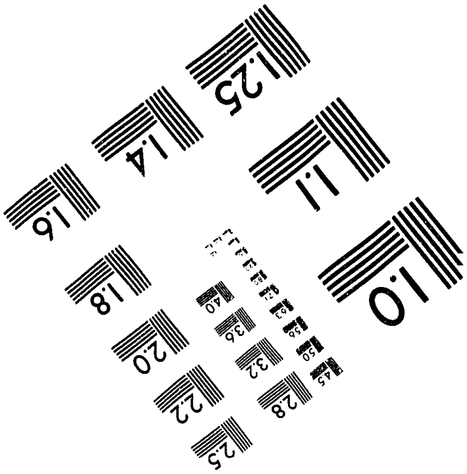

MANUFACTURED TO AIIM STANDARDS
BY APPLIED IMAGE, INC.

1 of 1

Conf-9301114--1

BNL-48498

DIFFUSE SCATTERING AND IMAGE CONTRAST OF TWEED IN SUPERCONDUCTING OXIDES: A SIMULATION AND INTERPRETATION

Yimei Zhu and Zhi-Xiong Cai
Materials Science Division, Brookhaven National Laboratory,
Upton, New York 11973, U.S.A.

DIFFUSE SCATTERING AND IMAGE CONTRAST OF TWEED IN SUPERCONDUCTING OXIDES: A SIMULATION AND INTERPRETATION

Yimei Zhu and Zhi-Xiong Cai
Materials Science Division, Brookhaven National Laboratory,
Upton, New York 11973, U.S.A.

ABSTRACT

Monte Carlo simulations were performed with a lattice gas model which represents the interactions between oxygen atoms in $YBa_2(Cu_{1-x}M_x)_3O_{7+\delta}$ (M=Fe, Co, or Al, $0.03<x<0.1$) system. The amplitudes of concentration waves / displacement waves obtained from these simulations then were used to calculate the intensity of the diffuse scattering of tweed seen in the electron diffraction pattern. The characteristic features of the tweed image were produced by calculation, using a model based on the contrast originating from structures with displacive modulation, stacking on the top of each other. Both calculations agree well with the TEM observations and provide an useful basis for a better insight into the origin of the tweed structure.

§1. Introduction

Tweed, a structural modulation, exhibits a roughly periodic lenticular domain image (Fig.1(a)) with associated streaks of diffuse scattering around the fundamental reflections in a diffraction pattern (Fig.1(b)). Tweedy modulation can be readily detected by transmission electron microscopy (TEM) for certain binary alloys, which usually present statistical fluctuations in their composition or in an order parameter.[1-5] In superconducting oxides, tweed (once proposed as possible flux-pinning centers) is observed in $YBa_2(Cu_{1-x}M_x)_3O_{7+\delta}$ (M=Fe, Co, or Al, $x > 0.025$, $\delta \sim 3x/2$),[6-10] and oxygen-reduced $YBa_2Cu_3O_{7-\delta}$ ($\delta \sim 0.6$-0.8),[11] i.e., for a composition where the superconductor appears to be tetragonal rather than orthorhombic from observing the fundamental reflections in diffraction experiments. The origin of tweed has been studied for many years, but is not completely understood. Recently, several groups carried out elegant experiments and analyses on tweedy modulation in $YBa_2Cu_3O_{7-\delta}$ system.[12-15] Skjerpe *et al.* proposed that (110) microtwins with orthorhombic symmetry are responsible for the macroscopic tetragonal symmetry in these alloyed superconductors,[12] while Jiang *et al.*. suggested that a random distribution of oxygen atoms in $YBa_2(Cu_{0.955}Al_{0.045})_3O_7$ would result in the diffuse streaks seen in diffraction.[13] On the other hand, Semenovoskaya *et al.* demonstrated that tweed structure is a metastable phase, and that the usual twin structure is formed by coarsening and refining the transient tweed structure.[14] To understand the origin of the tweed in $YBa_2(Cu_{1-x}M_x)_3O_{7+\delta}$, in this article, we report our observations and interpretation on tweed morphology, or image contrast, and its associated diffuse scattering made by computer simulations in real space and reciprocal space. For diffuse scattering, we used a displacement wave / concentration wave approach; the configuration of oxygen atoms was obtained by applying the Monte Carlo method to a lattice gas model.[15] For morphology, we used a simple model based on the contrast originating from structures with displaced domains stacked on top of each other along the c-axis. Our study clearly showed that the [110] and [-110] shear displacement produced by the short-range ordering or clustering of oxygen around the impurity atoms M on the Cu(1)-O "chain" plane is responsible for the formation of tweed in Fe-, Co-, or Al- alloyed $YBa_2Cu_3O_{7-\delta}$.

§2. Diffuse scattering

2.1 Observations

Fig.1(b) shows a selected area diffraction pattern of the [001] zone from a typical sample of $YBa_2(Cu_{0.97}Fe_{0.03})_3O_{7+\delta}$. The overall pattern has a four-fold symmetry and all the Bragg spots appear to be superimposed by two cross-streaks of same length in the [110] and [-110] directions. However, careful inspection of this figure reveals that the shapes of the diffuse scattering around the Bragg spots are not all identical. The lengths of the streaks increase with increasing distance from the origin. Furthermore, the radial streak at high-order [hh0] and [-hh0] reflections is shorter and weaker than the non-radial streak at the same spot. Such a difference is particular evident for a very thin sample, demonstrating the existence of strong double-diffraction effects, as is commonly observed in electron diffraction. One Bragg reflection may act as a new incident beam, i.e., the diffuse scattering at [uvw] is scattered by the [hkl] reflections into [uvw]+[hkl]. To minimize the double-diffraction effects, the number of reflections should be reduced to a minimum by tilting the sample away from zone axis. We found that when double diffraction is reduced, all [h00] and [0k0] reflections remain cross-shaped. Nevertheless, for all [hh0] and [-hh0] reflections the intensity of non-radial streaks remains strong, while the intensity of radial streaks disappears.[16] Thus, we conclude that the radial streak is due to double diffraction, while the other non-radial streaks reflect the nature of the tweed structure. The [001] diffraction pattern from tweed is illustrated in Fig.2, after removing the double-diffraction effect. The streaking of diffraction spots in reciprocal space can be attributed to a strain effect in real space. Due only to the strain, the shape of the diffuse scattering around the Bragg spot depends strongly on the index of that spot, and is zero at the origin. For a lattice with displacement vector **R**, streaks in the diffraction pattern will be visible through reflection **g** for which $\mathbf{R}\cdot\mathbf{g}\neq n$ (n=0,1,...) and invisible for $\mathbf{R}\cdot\mathbf{g}=0$.

2.2 Calculation

2.2.1 Oxygen ordering on a rigid lattice

The anisotropic lattice gas model for the $YBa_2(Cu_{1-x}M_x)_3O_{7+\delta}$ system is based on the assumption that the interaction between oxygen atoms can approximated by a metallically screened Columb interaction and that impurity doping and oxygen ordering happens only in the CuO basal plane.[17,18] This is reasonable for oxygen concentrations $\delta<0.5$. In addition to the Columb repulsion, two oxygen atoms bridged by a Cu atom also experience a short-range attraction due to covalent bonding. Since the elastic energy associated with lattice distortion is much smaller than the energy associated with the redistribution of oxygen between different lattice sites, the elastic energy can be treated as a perturbation of the lattice gas model Hamiltonian on a rigid lattice.

The structure of the CuO basal plane is approximated by a two-dimensional square lattice consisting of Cu atoms, oxygen atoms, and oxygen vacancies (Fig.3). When a di- or mono-valent Cu ion is replaced by an impurity ion M such as Fe, Co, or Al an extra hole will tend to localize near the M site, i.e., the M ion becomes effectively trivalent. This has two major effects: (a) the binding energy of an oxygen ion near the M site increases; and (b) the repulsion between oxygen atoms near the M site increases, due either to the increase of the negative change of oxygen ions or to the decrease on local screening. Based on this picture, the Hamiltonian representing the M-doped $YBa_2Cu_3O_{7-\delta}$ system is:

$$H=\sum_{\langle ij\rangle} V_{1ij}n_i n_j+V_2\sum_{(ij)b} n_i n_j+\sum_{(ij)a} V_{3ij}n_i n_j+\sum_i E_i n_i$$

where V_1, V_2, V_3 are the interaction parameters, E_i is the single-site binding energy, and n_i is the oxygen occupational operator.[17] The oxygen configuration near a single impurity atom M is shown in Fig.3. By minimizing the energy, the impurity atom forces the oxygen to form a short Cu-O chain along the a-axis, thus forming a local "cross-link" around the impurity site. Experimentally, the distribution of M ions is found to be uniform in sintered samples, therefore, we assume that the M atoms randomly occupy Cu sites.

Monte Carlo (MC) simulations were performed using Kawasaki dynamics. Lattice sizes ranging from 32×32 to 100×100 with periodic boundary conditions were used. The high temperature configuration was obtained by performing a MC simulation at T=2300K, and the system was equilibrated at this temperature with 10,000 MCS/site (MCS=Monte Carlo steps). The low temperature configurations were obtained by lowering the temperature of the system to 300 K in steps of 100K; 2,000 to 10,000 MCS/site were used to obtain the thermodynamic average for each temperature.

Fig.4 shows a typical oxygen and Fe configuration of $YBa_2(Cu_{2.97}Fe_{0.03})_3O_{7+\delta}$ with Fe randomly distributed. The local "cross-links" formed around Fe atoms disrupt the orthorhombic structure, and overall, the system shows a tetragonal symmetry. Since the oxygen atoms can be regarded as interstitial in CuO planes causing expansion of the lattice parameter in the direction of the Cu-O chain and contraction perpendicular to the Cu-O chain, the resulting lattice distortion caused by "cross-links" is along the [110] and [-110] directions.

2.2.2 Diffuse scattering arising from lattice displacement

Because the distortion of the lattice due to oxygen ordering is small, a linear elastic approximation can be used to study this distortion in the $YBa_2(Cu_{1-x}M_x)_3O_{7+\delta}$ system. At the long wave-length limit, the displacement of the lattices can be written to the first order as follows:[13,19]

$$\delta \boldsymbol{R}_S=\sum_q \boldsymbol{A}_q c_q \exp(-i\boldsymbol{q}\boldsymbol{R}_s)$$

where c_q is the amplitude of the planar oxygen-concentration wave with wave vector **q**. $\mathbf{A}_q$ is determined by three inhomogeneous linear equations:

$$q\lambda_{ijlm} n_j n_l A_{qm}=\lambda_{ijlm} n_j L_{lm}$$

where summation is made over repeated indices; λ_{ijlm} is a component of the elastic modulus tensor; n_j is a component of the unit vector $\mathbf{n}=q/q$, and L_{lm} is a component of the strain tensor describing the correlation between the lattice constant and the oxygen concentration of the CuO basal plane.

Once $\mathbf{A}_q$ is obtained from the above equation, we can derive the intensity of the diffuse scattering due to lattice distortion for a small displacement $\mathbf{q}$ of the scattering vector away from the fundamental reflection $\mathbf{Q}$[19]:

$$I_H(Q+q) = |F(Q)|^2 \, |Q\cdot(A_q^x c_q^x + A_q^y c_q^y)|^2$$

where c^x_q and c^y_q are the amplitudes of the oxygen concentration wave of two different kinds of interstitial oxygen atoms (along the b and a axis, respectively), and are obtained from the Monte Carlo simulation, and F(Q) is the atomic structure factor of the unit cell. The subscript, H, denotes the fact that this scattering intensity comes from generalized Huang scattering[19].

Since our TEM observations of diffuse scattering were made at room temperature, thermal diffuse scattering (TDS) also can make a major contribution to the total intensity of diffuse scattering. To the first-order approximation[20]:

$$I_{TDS} = |F(Q)|^2 \frac{kT}{v} \frac{(Q+q)^2}{q^2} K(f)_g$$

where T is the temperature, v is the volume of the unit cell, and $K(f)_g$ is the polarization factor. The total intensity of diffuse scattering is the sum of the thermal and Huang diffuse scattering, $I = I_H + I_{TDS}$.

In Fig.5, the calculated contour plots of diffuse scattering intensity around (040), (240), and (440) reflections are compared with the observed diffuse scattering in $YBa_2(Cu_{0.97}Cu_{0.03})_3O_{7+\delta}$. Fig.5(a)-(c) shows the calculated intensity, I_H, caused by lattice displacement only, and Fig.5(d)-(f) shows the calculated total diffuse scattering intensity, I, due to lattice distortion and thermal vibration. Fig.5 (g)-(i) are the experimental observations. The calculated intensity profiles agree very well with the TEM data suggesting that lattice distortion due to oxygen ordering gives rise to the streaks of the diffuse scattering, as qualitatively shown in Fig.2.

§3. Image contrast

3.1 Observations

Tweed contrast also obeys the $\mathbf{g}\cdot\mathbf{R}=0$ extinction rule. In bright- and dark-field imaging near the (001) zone, tweed contrast shows up as fine striations along the [110] and [-110] directions for a (h00) reflection (Fig.1(a)), while, for a (hh0) reflection only one set of striations parallel to the diffraction vector is visible (Fig.6). This observation again suggests that tweed contrast is a strain contrast, and reflects the characteristic features of a quasi-periodic structure modulation. However, it has been argued that the contrast is simply an artifact[5] by observing the variation in tweed width with the deviation from the Bragg reflection, s, in Ni-Al alloy. But our observations show this is not the case in alloyed $YBa_2Cu_3O_{7-\delta}$, the average tweed spacing only varies with M concentration from 4 nm for x=0.03 to smaller than 1.5 nm for x>0.1[21], and is relatively *independent* of diffraction conditions. Figures 6(a)-(g) are dark-field images of $YBa_2(Cu_{1-x}M_x)_3O_{7+\delta}$ (M=Fe, x=0.03) from the same area under the diffraction conditions of $\mathbf{g}_{110}/\mathbf{g}_{hh0}$ (imaged by $\mathbf{g}_{110}$ while $\mathbf{g}_{hh0}$ is excited, where hh0=110, 220, 440, (see inset, Fig.6(a)-(g))). By increasing the deviation s ($|s|$ = 0.00038 ~ 0.0055 $Å^{-1}$ was accurately measured by the distance of the corresponding Kikuchi line from the Bragg spot) from the Bragg position for a (hh0) reflection, the thickness fringes come closer together indicating that there is a decrease in the effective extinction distance, ξ_g. To check the change of the tweed width with s, optical diffractograms Fourier-transformed from the images of Fig.6(a)-(g) were analyzed by shining a laser beam on the film negatives. The reciprocal streaks, which are perpendicular to the tweed domain in real space, showed no remarkable difference for all the values of s used. The analysis of the diffractograms suggests that the typical dimension of the domain for $YBa_2(Cu_{0.97}Cu_{0.03})_3O_{7+\delta}$ is about 4 nm across and 35 nm along the tweed.[22]

3.2 Calculation

3.2.1 Overlapped orthorhombic domains

Our Monte Carlo simulation showed that tweed structure in real space consists of short-range ordering or clustering of oxygen. Such ordering can be described as small orthorhombic microdomains, the size of which is determined by the Cu-O chain cross-links around M impurities. On the other hand, the broadening of the reflections in electron diffraction suggests that the coherence length of these domains is typically 10-30 nm along the c-axis. Thus, they are expected to overlap for an average thickness of 20-100 nm of a TEM sample. Several domains stacking on top of each other contribute to the contrast when the incident electron beam is nearly parallel to the c-axis in two-beam imaging.

3.2.2 Image contrast arising from the overlapped domains

Tweed contrast can be calculated by considering the displacement of the lattice planes, **R**, relative to each other in the stacked domains. The so-called kinematical calculations give the same result as two-beam dynamical calculations when the deviation from the Bragg position, s, is sufficiently large. The amplitude of the scattered wave Φ_g at the bottom surface of the crystal is:

$$\Phi_g = \frac{i\pi}{\xi_g}\int_0^t e^{-2\pi i \mathbf{g}\cdot\mathbf{R}} e^{-2\pi i s z} dz$$

where ξ_g is the extinction distance, t is the total thickness of the foil, **g** is the diffraction vector used for imaging, and z is the distance from the center of the foil to the fault, measured along the direction of the incident beam.[23] The intensity of the reflected beam, i.e. the dark-field image, can be expressed by:

$$I = \frac{1}{(\xi_g s)^2}\left[\sin^2(\pi ts+\pi \mathbf{g}\cdot\mathbf{R}) + \sin^2(\pi \mathbf{g}\cdot\mathbf{R}) - 2\sin(\pi \mathbf{g}\cdot\mathbf{R})\sin(\pi ts+\pi \mathbf{g}\cdot\mathbf{R})\cos 2\pi sz\right]$$

Fig.7 shows examples of the contrast calculations. For a perfect crystal of constant thickness there is no contrast, Fig.7(a), while for a stacking fault with a constant displacement vector **R** running from top to bottom in a foil of constant thickness, Fig.7(b), we see the oscillation of contrast with depth of the fault. When **R** varies as a function of position **x**, we obtain the modulated contrast shown in Figs.7(c)-7(e), with various deviations from the Bragg position, s=3.25/t (Fig.7(c)), s=3.5/t (Fig.7(d)), and s=5.5/t (Fig.7(e)). In these calculations, we used a simple sinusoidal wave as a [110] displacive modulation for **R**. All the intensity profiles were calculated for a modulation with a period of 8 nm (the domain size is half of the period). The tweed contrast calculated for a different period (4 nm, $s=3.25/t$) is shown in Fig.7(f). Here, the length of the tweed is limited by the effective extinction distance, ξ_p which is the same order as domain size on the a-b plane. By using more complicated wave functions for **R**, a quasi-periodic tweed contrast can be generated, as shown in Fig.7(g).

Our image calculation (Fig.7) generated strain contrast similar to that observed from tweed structure, also confirming that: (1) the intensity of the tweed image decreases with period; (2) the width of the tweed is independent of the deviation from the Bragg position, s, although here, the situation is more complicated for small s where the kinematical treatment does not apply. Analysis of Fig.6(a) and (b) reveals a large variability in tweed spacing when a small deviation s used in imaging. A similar observation was made by Robertson and Wayman[4] in Ni-Al alloy system. However, we attribute the appearance of the wider striation of tweed contrast in Fig.6(a) and (b) to poorer resolution close to the Bragg position where the effective extinction distance, ξ_p is larger because the two-beam image resolution of a defect is usually approximately $\xi_g/3$.[24] Thus, the contrast caused by more than one interface lying on top of another within the foil may not be separated when s becomes small. For most imaging conditions, the number of the domains interfaces on the top of each other may not be important, and the observation of only minor changes in the tweed contrast with thickness suggests that the regions near the surfaces mainly contribute to the contrast, similar to the case for stacking faults, where absorption tends to reduce the contrast in the interior of the foil.

§4. Conclusion

We have successfully simulated the image and diffuse scattering of tweed in $YBa_2(Cu_{1-x}M_x)_3O_{7+\delta}$ ($M=$Fe, Co, or Al, $0.03 < x < 0.1$) based on observations by transmission electron microscopy. Our results show that lattice displacement gives rise to the tweed image contrast, as well as to the streaks of diffuse scattering around the fundamental reflections in electron diffraction. We also demonstrated that small orthorhombic domains associated with oxygen "cross-links" near impurity atoms M is the direct cause of the (110) and the equivalent (-110) lattice distortion in the tweedy superconducting oxides. In other systems, tweed structure also may commonly undergo similar characteristic displacive modulation.

Acknowledgment

We would like to thank J. Tafto, S.C. Moss, and A.G. Khachaturyan for stimulating discussions, and M. Suenaga and D.O. Welch for encouragement and discussions. This research was performed under the auspices of the U.S. Department of Energy, Division of Materials Sciences, Offices of Basic Energy Sciences under Contract No. DE-AC02-76CH00016.

REFERENCE

1. L.E. Tanner, *Phil.Mag.A*, **14**, (1966) 111.

2. L.E. Tannar, A.R. Pelton, and R. Gronsky, *J. Phys. Paris*, **43**, Suppl, 12, (1982), C4-169.

3. A.G. Khachaturyan, *Theory of Structure Transformations in Solids* New York: John Wiley, (1983).

4. I.M. Robertson, and C.M. Wayman, *Phil.Mag.A*, **48** (1983) 421, 443, 629.

5. S.M. Shapiro, J.Z. Larese, Y. Noda, S.C. Moss, and L.E. Tanner, *Phys.Rev.Lett.*, **57**, (1986) 3199.

6. S. Iijima, T. Ichihashi, Y. Kubo, and T. Tabuchi, *Jpn.J.Appl.Phys.*, **26**, (1987) L1790.

7. Z. Hiroi, M. Takano, Y. Takeda, R. Kanno, and Y. Bando, *Jap.J.Appl.Phys.*, **27**, (1988) L580.

8. Y. Xu, M. Suenaga, J. Tafto, R.L. Sabatini, A.R. Moodenbaugh, and P. Zolliker, *Phys.Rev.B*, **39**, (1989) 6667.

9. W.W. Schmahl, A. Putnis, E. Salje, P. Freeman, A. Graeme-Barber, R. Jones, K.K. Singh, J. Blunt, P.P. Edwards, J. Loram, and K. Mirza, *Phil.Mag,lett.* **60**, (1989) 241.

10. T. Kreckels, G. Van Tendeloo, D. Broddin, S. Amelinckx, L.E. Tanner, M. Menbod, E. Vanlathem, and R. Deltour, *Physica C*, **173**, (1991) 361.

11. Y. Zhu, M. Suenaga, and A.R. Moodenbaugh, *Phil. Mag. Lett.*, **62**, (1990) 51.

12. P. Skjerpe, A. Olsen, J. Tafto, M. Suenaga, Y. Zhu, and A.R. Moodenbaugh, *Phil.Mag.B*, **65** (1992) 1067.

13. X. Jiang, P. Wochner, S.C. Moss, P. Zschack, *Phys.Rev.Lett.*, **67**, (1991) 2167

14. S. Semenovskaya, and A.G. Khachaturyan, *Phys. Rev. Lett.* **16** (1991) 2223; *Phys. Rev. B* **46** (1992) 6511.

15. Z.-X. Cai, Y. Zhu, and D.O. Welch, *Phys. Rev. B*, **46** (1992) 11014.

16. Y. Zhu, M. Suenaga, and J. Tafto, *Phil. Mag. Lett.*, **64**, (1991) 29.

17. D. de Fontaine, L.T.Wille, and S.C. Moss, *Phys. Rev. B*, **36** (1987) 5709.

18. Z.-X. Cai and S.D. Mahanti, *Sol. St. Comm.* **67**, (1988) 287; *Phys. Rev. B*, **40** (1989) 6558.

19. M.A. Krivoglaz, *Theory of X-ray and Thermal Neutron Scattering by Real Crystals*, Plenum Press, New York (1969).

20. W.A. Wooster, *Diffuse X-ray Reflections From Crystals*, Clarendon Press, 1961.

21. Y. Zhu, M. Suenaga, and A.R. Moodenbaygh, *Ultramicroscopy*, **37**, (1991) 341.

22. Y. Zhu, M. Suenaga and J. Tafto, *Philo. Mag. A* (1992), in press.

23. P.B. Hirsch, A. Howie, P.B. Nicholson, D.W. Pashley, and M.J. Whelan, *Electron Microscopy of Thin Crystals* London: Butterworths, (1965).

24. G. Thomas, and M. Gorinqe, *Transmission Electron Microscopy of Materials*, (1979) p37.

Figure Captions

Fig.1

(a) Tweed contrast in $YBa_2(Cu_{0.97}Fe_{0.03})_3O_{7+\delta}$, imaged under **g**=200 two-beam condition. (b) a (001) selected-area diffraction pattern from (a).

Fig.2

A schematic drawing of the [001] diffraction pattern in $YBa_2(Cu_{1-x}M_x)_3O_{7+\delta}$ (M=Fe, Co, and Al, $0.03 < x < 0.1$). The solid streaks and the dashed streaks correspond to the [110] and [-110] structural modulation, respectively. Note, there are no radial streaks.

Fig.3

Structure of the basal plane of $YBa_2(Cu_{1-x}M_x)_3O_{7+\delta}$ with a single M impurity. V_1 is the interaction parameter between nearest-neighbor oxygen atoms; V_2 is the interaction parameter between next-nearest-neighbor oxygen atoms bridged by Cu; and V_3 is the interaction parameter between next-nearest-neighbor oxygen atoms not bridged by Cu.

Fig.4

An atomic configuration of the $YBa_2(Cu_{0.97}Cu_{0.03})_3O_{7+\delta}$ basal plane obtained by Monte Carlo simulation of a 32×32 lattice with periodic boundary conditions at 300K. The Fe atoms are randomly distributed. The small diamonds indicate Cu positions, the small circles indicate oxygen position, and the large diamond indicate Fe positions.

Fig.5

Calculated and observed diffuse scattering in $YBa_2(Cu_{0.97}Cu_{0.03})_3O_{7+\delta}$ around (040), (240) and (440) Bragg spots. (a)-(c) due to Huang scattering (lattice displacement); (d)-(f) the combined Huang scattering and thermal diffuse scattering; (g)-(i) the TEM observations. Note, the contour plots are in logarithmic intervals.

Fig.6

g=110 dark field images of $YBa_2(Cu_{0.97}Fe_{0.03})_3O_{7+\delta}$ for different deviations, s, from the Bragg position. (a) s=-0.00038 $Å^{-1}$; (b) s=0.0013 $Å^{-1}$; (c) s=0.0017 $Å^{-1}$; (d) s=0.0021 $Å^{-1}$; (e) s=0.0035 $Å^{-1}$; (f) s=0.0050 $Å^{-1}$, and (g) s=0.0055 $Å^{-1}$.

Fig.7

Two-beam dark field images from a domain interface with displacement, **R**, when the interface run from top to bottom: (a) $|\mathbf{R}| = 0$; (b) $|\mathbf{R}|$ = constant; (c)-(f) $|\mathbf{R}| = f(\sin x)$, for different period p and different deviations from the Bragg position s: (c) p=8 nm, s=3.25/t; (d) p=8 nm, s=3.5/t; (e) p=8 nm, s=5.5/t; (f) p=4 nm, s=3.25/t; (g) $|\mathbf{R}| = f_1(\sin x)+f_2(\sin x)$, s=1/t.

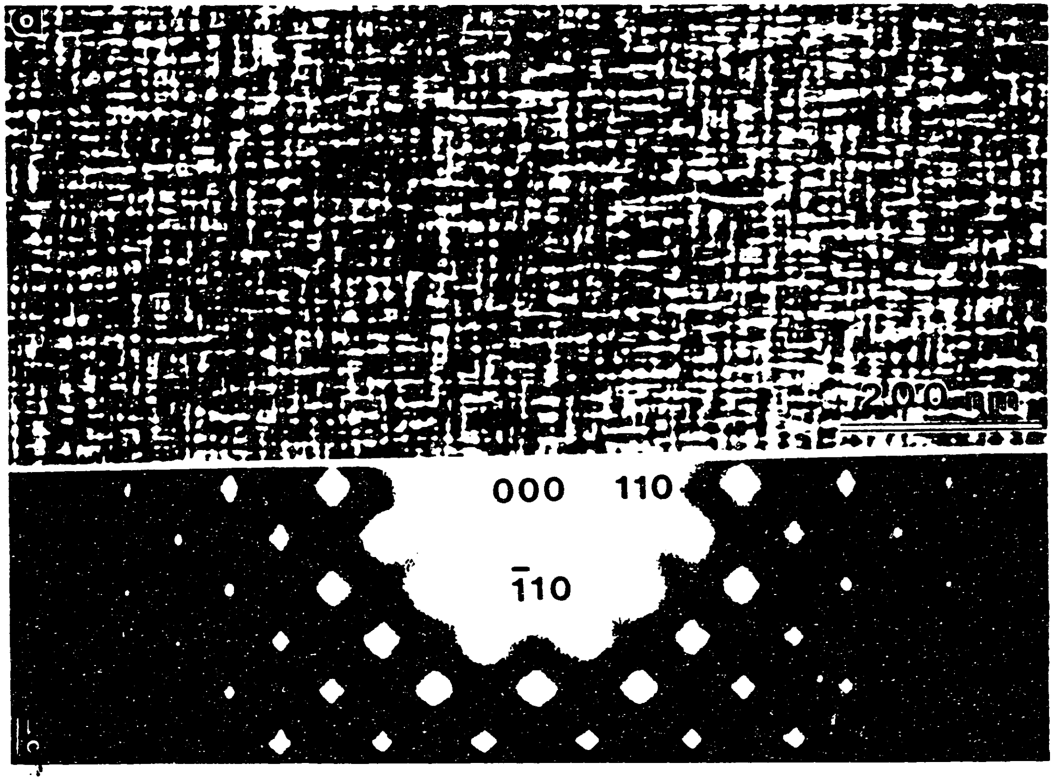
a
200 nm
000
110
$\bar{1}10$
c

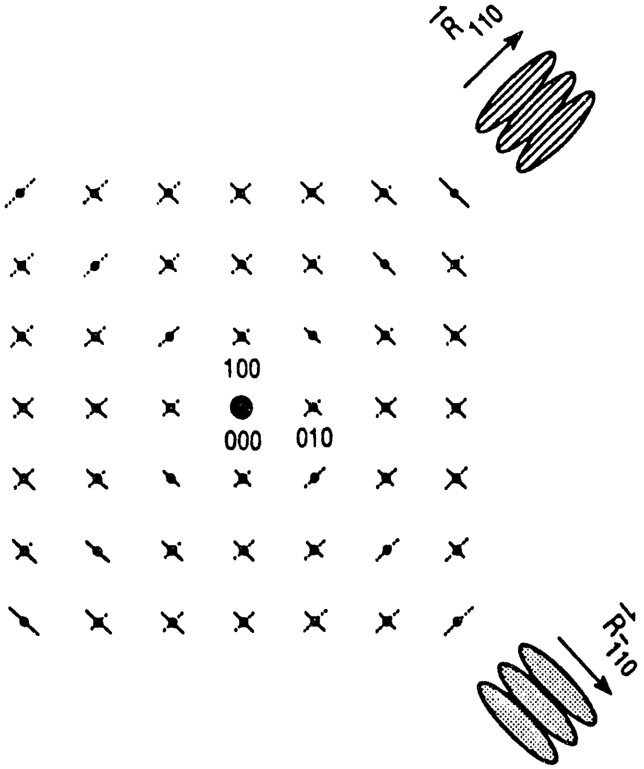

Zhu 3a 11/13/90 j.p.

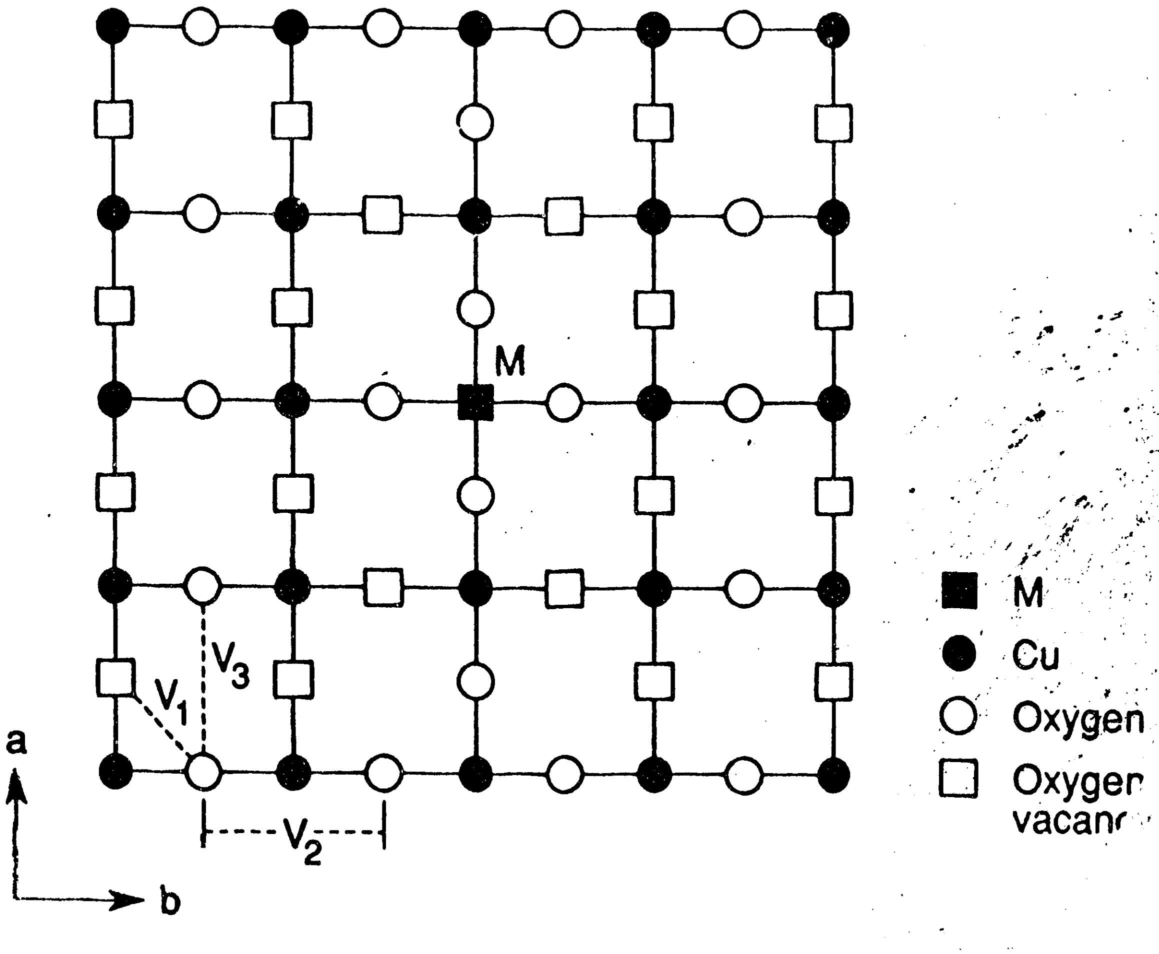
M
V$_3$
V$_1$
V$_2$
a
b
M
Cu
Oxygen
Oxygen
vacanc

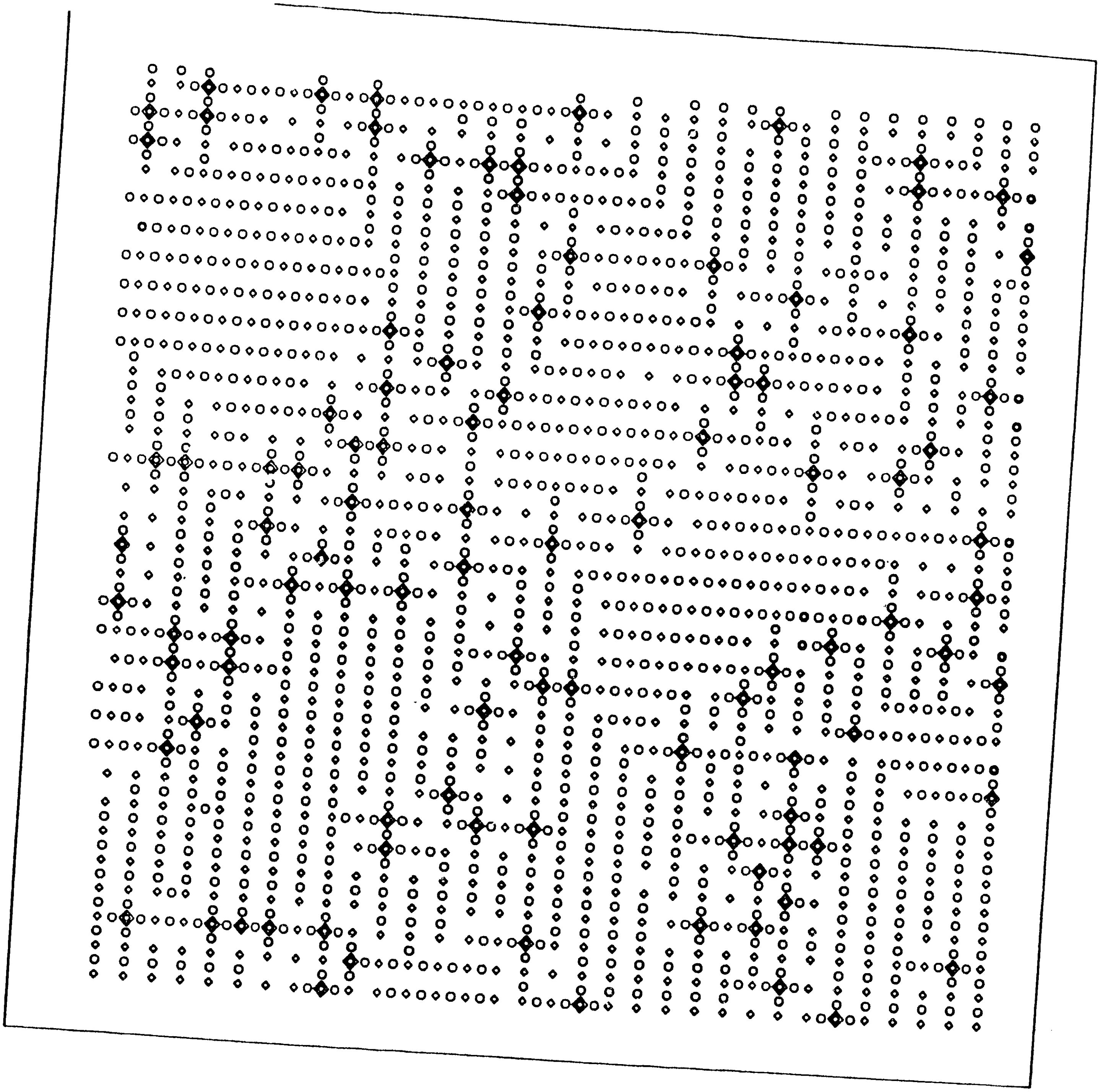

4

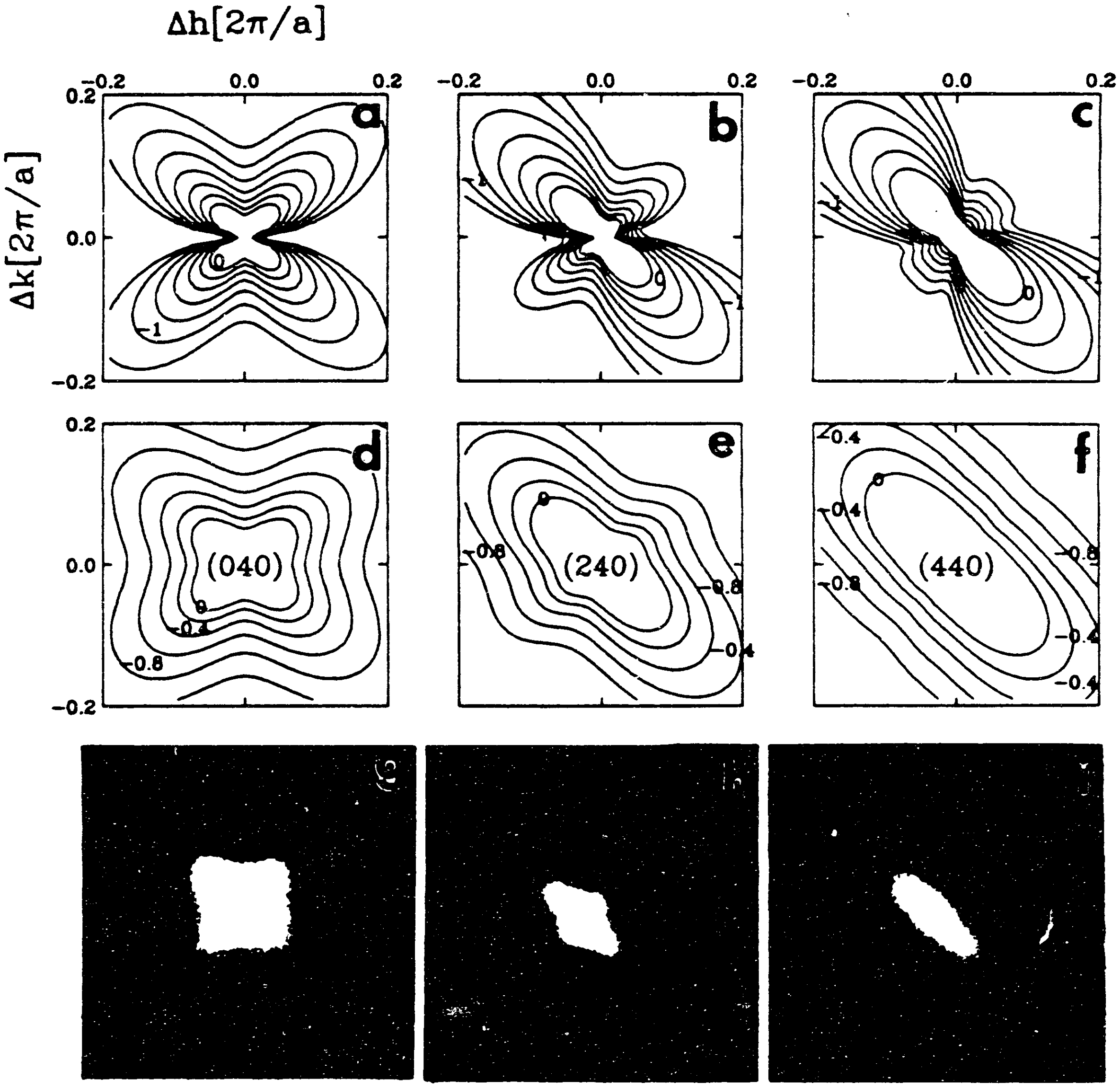
Δh[2π/a]
Δk[2π/a]
−0.2
0.0
0.2
a
b
c
d
e
f
g
h
i
0
−1
(040)
(240)
(440)
−0.4
−0.8

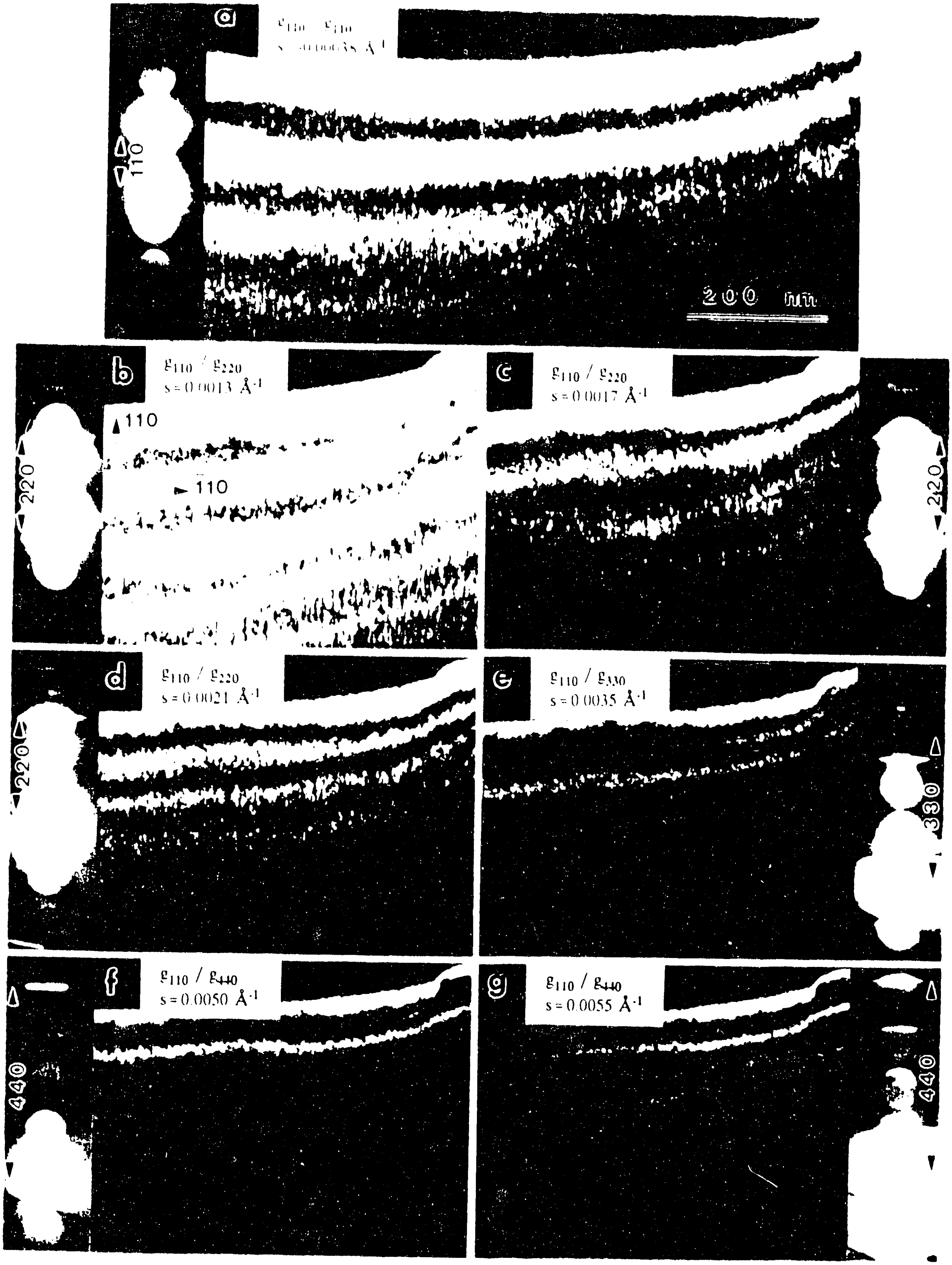a
g110 / g110
s = -0.00035 Å-1
110
200 nm
b
g110 / g220
s = 0.0013 Å-1
110
110
220
c
g110 / g220
s = 0.0017 Å-1
220
d
g110 / g220
s = 0.0021 Å-1
220
e
g110 / g330
s = 0.0035 Å-1
330
f
g110 / g440
s = 0.0050 Å-1
440
g
g110 / g440
s = 0.0055 Å-1
440

t

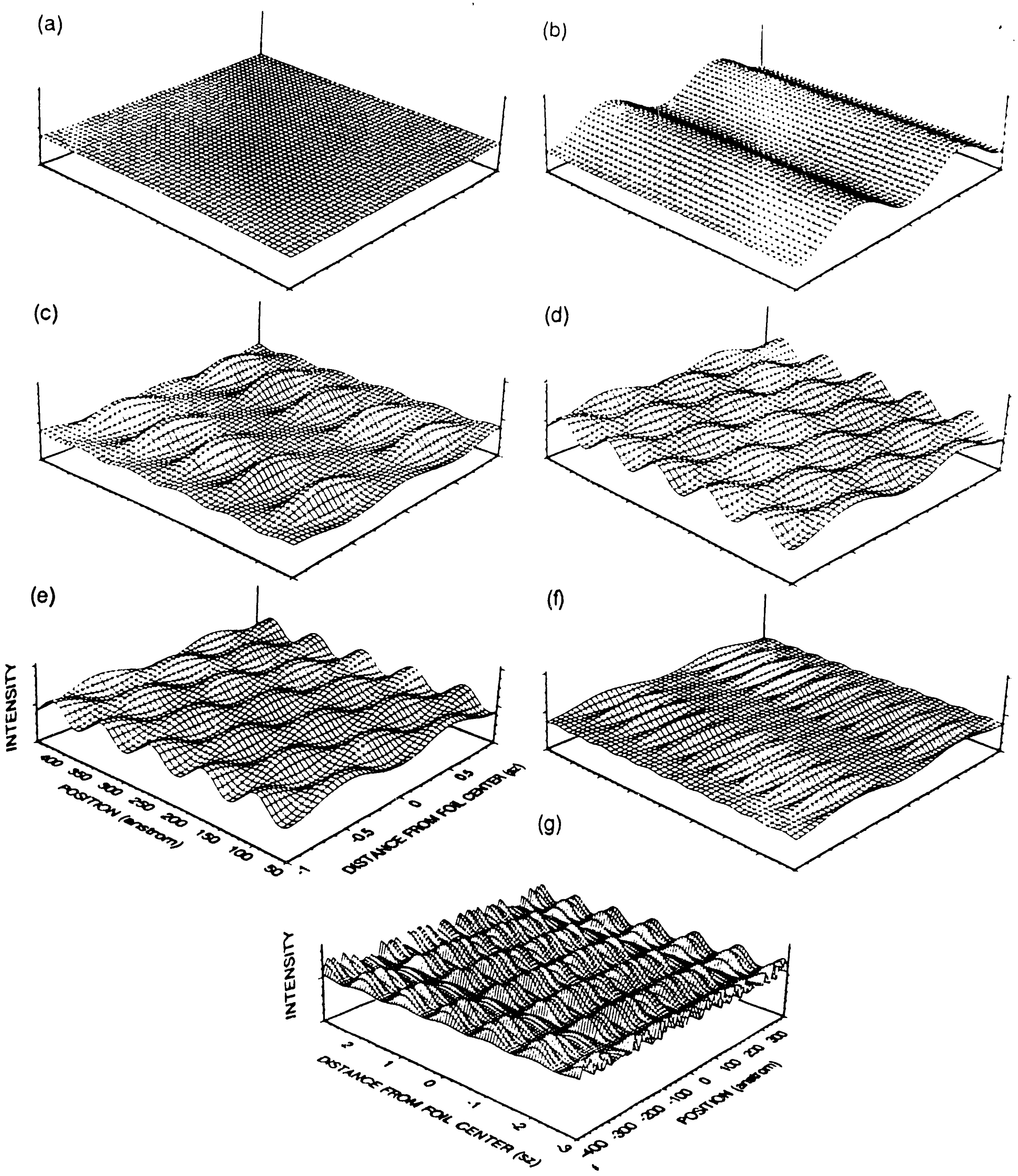
(a)
(b)
(c)
(d)
(e)
(f)
(g)
INTENSITY
400 350 300 250 200 150 100 50
POSITION (anstrom)
-1 -0.5 0 0.5
DISTANCE FROM FOIL CENTER (sz)
INTENSITY
2 1 0 -1 -2 -3
DISTANCE FROM FOIL CENTER (sz)
-400 -300 -200 -100 0 100 200 300
POSITION (angstrom)

DATE
FILMED

8/23/93

END